

# Photoluminescent Layered Y(III) and Tb(III) Silicates Doped with Ce(III)

Mariya H. Kostova,<sup>†</sup> Rute A. Sá Ferreira,<sup>‡</sup> Duarte Ananias,<sup>†,§</sup> Luís D. Carlos,<sup>\*,‡</sup> and João Rocha<sup>\*,†</sup>

Department of Chemistry, and Department of Physics, CICECO, University of Aveiro, 3810-193 Aveiro, Portugal, and Department of Biochemistry, NMR Centre and Centre of Neurosciences and Cell Biology, University of Coimbra, 3001-401 Coimbra, Portugal

Received: May 5, 2006; In Final Form: June 6, 2006

The synthesis and structural characterization of new layered rare-earth silicates  $K_3[M_{1-a}Ce_aSi_3O_8(OH)_2]$ ,  $M = Y^{3+}, Tb^{3+}$ ,  $a \ll 1$  (AV-22 materials), have been reported. These materials combine the properties of layered silicates, such as intercalation chemistry, and photoluminescence and may find applications in new types of sensor devices. For mixed Tb/Ce-AV-22, evidence has been found for the energy transfer from the large  $Ce^{3+} 4f^1 \rightarrow 5d^1$  broad band to the sharp  $Tb^{3+} 4f^8$  lines. This energy transfer allows the fine-tuning of the color emission in the blue-green region of the chromaticity diagram. Upon  $Ce^{3+}$  excitation (342 nm), the radiance of Tb/Ce-AV-22 is approximately 2 times higher than that measured under direct  $Tb^{3+}$  excitation, which reinforces the existence of effective room-temperature  $Ce^{3+}$ -to- $Tb^{3+}$  energy transfer.

## 1. Introduction

Layered<sup>1</sup> microporous silicates are host–guest systems suitable for engineering multifunctional materials with tuneable properties.<sup>2,3</sup> In particular, it has been shown that solids combining the properties of layered silicates (intercalation chemistry) or zeolites (such as ion exchange and molecular sieving) and photoluminescence (PL) may be obtained by inserting  $Ln^{3+}$  cations into the frameworks, layers, micropores, and interlayer spaces.<sup>4</sup> While research into zeolites made photoluminescent by Ln-doping via ion-exchange is not new, the preparation of layered and zeolite-type stoichiometric Ln silicates is an emerging field.<sup>5</sup>

Because the  $4f^1 \rightarrow 5d^1$  transition of  $Ce^{3+}$  is parity allowed, its absorption cross section is much larger than that of the intra- $4f$  lines, and thus this ion may act as an  $Ln^{3+}$  sensitizer. The  $Ce^{3+}$ -to- $Ln^{3+}$  (mainly  $Tb^{3+}$ ) energy transfer has been much studied in the past decades and shown to depend on the host lattice and the extent of the overlap between the  $Ce^{3+}$  emission and the  $Tb^{3+}$  excitation spectrum.<sup>6–10</sup> In this context, one of the main motivations has been the development of new, highly efficient, green-emitting phosphors to be used in the low-pressure mercury vapor lamps.  $Ce^{3+}$ -containing materials also find potential applications in optoelectronics.  $Ce^{3+}$  in a  $LiY_6$  matrix has been shown to lase, and this is particularly important because  $Ce^{3+}$  lasers emit in the blue or ultraviolet and exhibit tunability, due to the inherently broad emission lines.<sup>11</sup> A microporous, stoichiometric, photoluminescent cerium silicate has also been described.<sup>3</sup>

Recently, we have reported the synthesis, structure, and PL properties of mixed layered Ln silicates  $K_3[M_{1-a}Ln_aSi_3O_8(OH)_2]$ ,  $M = Y^{3+}, Tb^{3+}$ ,  $Ln = Eu^{3+}, Er^{3+}, Tb^{3+}$ , and  $Gd^{3+}$ , named AV-22 materials.<sup>1</sup> Building upon this work, we now wish to report on the related system  $K_3[M_{1-a}Ce_aSi_3O_8(OH)_2]$ ,  $M = Y^{3+}, Tb^{3+}$ ,

$a \ll 1$ . The emission spectra, the (x,y) chromaticity coordinates, radiance, and time-decay measurements clearly show that the incorporation of  $Ce^{3+}$  and  $Tb^{3+}$  ions into the same layered silicate induces an effective  $Ce^{3+}$  to  $Tb^{3+}$  energy transfer channel.

## 2. Experimental Methods

**2.1. Synthesis.** The syntheses of AV-22 materials have been described.<sup>1</sup> In a typical  $K_3[TbSi_3O_8(OH)_2]$  synthesis, an alkaline solution was made by mixing 1.24 g of precipitate  $SiO_2$  (93% m/m  $SiO_2$ , Riedel-de Haën), 20.32 g of  $H_2O$ , and 9.12 g of KOH (Merck). An amount of 0.82 g of  $TbCl_3 \cdot 6H_2O$  (Aldrich) was added to this solution, and the mixture was stirred thoroughly. The gel, with composition  $4.23 K_2O:1.0 SiO_2:0.06 Tb_2O_3:58 H_2O$  was transferred to Teflon-line autoclaves, and the hydrothermal synthesis was carried out under autogenous pressure for 7 days at 230 °C. The obtained microcrystalline powders were filtered, washed at room temperature with distilled water, and dried at 100 °C. Mixed Y/Ce and Tb/Ce were prepared by introducing in the parent gel 5% Ce.

**2.2. Characterization.** Within experimental error, chemical analysis by EDS confirmed the K:Ln:Si ( $Ln = Y$  or  $Tb$ ) molar ratios obtained by powder XRD, ca. 3:1:3. ICP-AES chemical analysis yielded ca. 3.2 and 2.1 mol % Ce for, respectively, the Tb/Ce and Y/Ce samples, despite the fact that larger Ce amounts were present in the parent synthesis gel. All AV-22 materials were characterized by powder X-ray diffraction (XRD) on an X'Pert MPD Philips diffractometer (Cu  $K\alpha$  radiation) fitted with a curved graphite monochromator and scanning electron microscopy (SEM) performed on a Hitachi S-4100 microscope. Y-AV-22 was also characterized by  $^{29}Si$  magic-angle spinning (MAS) NMR.

The photoluminescence (PL) and lifetimes measurements were recorded on a Fluorolog-3 (FL3-2T model) with double excitation spectrometer, fitted with a 1200 grooves/mm grating blazed at 330 nm, and a single emission spectrometer (TRIAX 320), fitted with a 1200 grooves/mm grating blazed at 500 nm, coupled to a R928P photomultiplier. The excitation sources were

\* Corresponding author. Phone: +351234370946. Fax: +351 234424965. E-mail: lcarlos@fis.ua.pt (L.D.C.); rocha@dq.ua.pt (J.C.R.).

<sup>†</sup> Department of Chemistry, University of Aveiro.

<sup>‡</sup> Department of Physics, University of Aveiro.

<sup>§</sup> University of Coimbra.

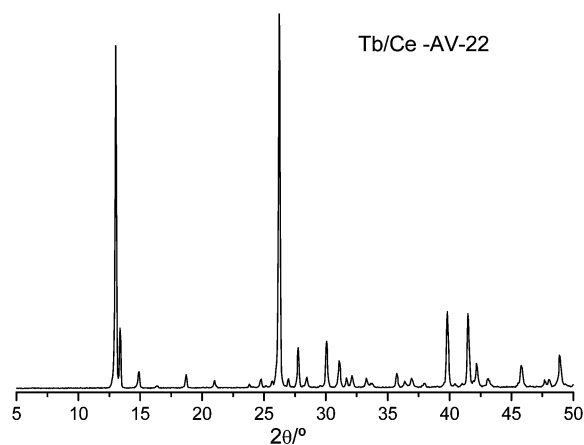


Figure 1. Powder XRD pattern of Tb/Ce-AV-22.

a 450 W Xe arc lamp and pulsed Xe–Hg lamps for the steady-state and time-resolved measurements, respectively. Excitation spectra were corrected from 240 to 600 nm for the spectral distribution of the lamp intensity using a photodiode reference detector. On the basis of the excitation source characteristics, we estimate that the intensity of the spectrum recorded in the 200–240 nm region should be multiplied by a factor of 2. Emission spectra were also corrected for the spectral response of the monochromators and the detector using typical correction spectra provided by the manufacturer. The measurements at 14 K were performed using a He closed-cycle cryostat. The radiance measurements and the CIE (*x*,*y*) emission color coordinates were performed using a telescope optical probe (TOP 100 DTS140-111, Instrument Systems). The excitation source was a Xe arc lamp (150 W) coupled to a Jobin Yvon-Spex monochromator (TRIAX 180). The width of the rectangular excitation spot was set to 2 mm and the diameter used to collect the emission intensity to 0.5 mm, thus ensuring that the entire sample was illuminated. The emission color coordinates and the radiance of the standard green phosphor Gd<sub>2</sub>O<sub>2</sub>S:Tb (Phosphor Technology) were also measured exciting at 270 nm. Since the radiance will depend on the surface density of the emitting centers, care was also taken in preparation of the samples; pellets with a thickness around 0.8 mm containing the same amount and compaction degree were made. The radiance values were corrected for the spectral distribution of the lamp intensity. The experimental error is within 5%.

All materials studied display powder XRD patterns characteristic of AV-22 (Figure 1), and no evidence was found for the presence of any impurity phases. No significant changes in the unit cell parameters or crystallite morphology were observed upon Ce<sup>3+</sup> incorporation. The <sup>29</sup>Si MAS NMR spectra of Y- and Y/Ce-AV-22 (not shown) are also typical of AV-22 materials.

### 3. Results and Discussion

**3.1. Structural Data.** To assist the discussion of the PL results, the structure of AV-22 materials is now briefly described (Figure 2). An orthorhombic unit cell (*a* = 13.210(3), *b* = 13.543(3), *c* = 5.9072(12) Å) and space group *Pnma* for Tb-AV-22 have been previously reported.<sup>1</sup> Ln-AV-22 contains a single crystallographic Ln<sup>3+</sup> center (a slightly distorted LnO<sub>6</sub> octahedron) coordinated to six SiO<sub>4</sub> tetrahedra. There are two independent silicon tetrahedra: SiO<sub>4</sub>H establishes corner-sharing bridges between adjacent LnO<sub>6</sub> octahedra, leading to the formation of one-dimensional arrays running along the *c* axis

direction; SiO<sub>4</sub> units share corners with two SiO<sub>4</sub>H tetrahedra and two LnO<sub>6</sub> octahedra, linking adjacent one-dimensional arrays and leading to the formation of a two-dimensional [LnSi<sub>3</sub>O<sub>8</sub>(OH)<sub>2</sub>]<sub>*n*</sub><sup>3*n*−</sup> anionic perforated plane net perpendicular to the *b* direction. The crystal structure of Tb-AV-22 may be described as the parallel packing in an [ABAB...] fashion along the *b* axis direction of [LnSi<sub>3</sub>O<sub>8</sub>(OH)<sub>2</sub>]<sub>*n*</sub><sup>3*n*−</sup> anionic layers (two per *b* axis), which are further interconnected through strong O–H...O hydrogen bonds between neighboring Si–OH groups. There are two crystallographically unique charge-balancing K<sup>+</sup> cations: K(1) resides within the pores of the [LnSi<sub>3</sub>O<sub>8</sub>(OH)<sub>2</sub>]<sub>*n*</sub><sup>3*n*−</sup> layers, while K(2) occupies the interlayer space. The Ln<sup>3+</sup> ions residing in the layers and the K(1) ions are both located in a mirror plane of the *Pnma* (*D*<sub>2*h*</sub>) space group, whereas K(2) ions are in a generic crystallographic position.

**3.2. Photoluminescence Spectroscopy.** The room-temperature excitation spectra of Tb/Ce-AV-22 materials (Figure 3A) display a series of sharp Tb<sup>3+</sup> lines, ascribed to the intra 4f<sup>8</sup> transitions between the <sup>7</sup>F<sub>6</sub> and <sup>5</sup>G<sub>4–6</sub>, <sup>5</sup>L<sub>9,10</sub>, <sup>5</sup>D<sub>2–4</sub> levels, superimposed on a broad band in the range 300–360 nm, also observed in the spectra of Y/Ce materials, and ascribed to the Ce<sup>3+</sup> 4f<sup>1</sup> → 5d<sup>1</sup> transition. The two broad bands at 236 and 250–290 nm are assigned to, respectively, the spin-allowed (low-spin, LS) and spin-forbidden (high-spin, HS) interconfigurational Tb<sup>3+</sup> fd transitions.<sup>10,12,13</sup> Figure 3B shows the 14 K excitation spectrum of Tb/Ce-AV-22, monitored at the <sup>5</sup>D<sub>4</sub> → <sup>7</sup>F<sub>5</sub> transition (543 nm) and at 420 nm. Although the room-temperature and 14 K excitation spectra of Tb/Ce-AV-22 are similar, the intensity of the Ce<sup>3+</sup> 4f<sup>1</sup> → 5d<sup>1</sup> transition increases relative to the sharp Tb<sup>3+</sup> lines and the <sup>7</sup>F<sub>6</sub> → <sup>5</sup>G<sub>5,6</sub>, <sup>5</sup>L<sub>10</sub> transitions are better seen. The spectrum monitored at 420 nm displays only the broad Ce<sup>3+</sup> 4f<sup>1</sup> → 5d<sup>1</sup> band. Again, this transition is clearly present in the 14 K excitation spectrum of the Y/Ce sample. This band displays three components at ca. 345, 323, and 313 nm originated from transitions from the <sup>2</sup>F<sub>5/2</sub> level of the ground state to the crystal field split 5d level components (see energy scheme in Figure 3B). The HS band shows three components at ca. 282, 267, and 262 nm due to the crystal field splitting of the 5d configuration, and the energy separation between the LS and HS fd transitions (ca. 7320 cm<sup>−1</sup>) is very similar to the energy separation reported before for Tb-AV-22.<sup>1</sup> The presence of the Ce<sup>3+</sup> 4f<sup>1</sup> → 5d<sup>1</sup> transition in the excitation spectrum monitored within the Tb<sup>3+</sup> 4f<sup>8</sup> lines indicates that the Ce<sup>3+</sup>-to-Tb<sup>3+</sup> energy transfer channel is active in the range 14–300 K, being more efficient at low temperature. The Ce<sup>3+</sup> to Tb<sup>3+</sup> energy transfer is also evidenced by the decrease of the relative intensity of the Tb<sup>3+</sup> 4f<sup>8</sup> → 4f<sup>7</sup>5d<sup>1</sup> lines as compared to the lines of Tb-AV-22.<sup>1</sup> This observation has been previously reported<sup>10</sup> and suggests that the excitation of Tb<sup>3+</sup> occurs mainly through the excitation of Ce<sup>3+</sup>. Because of the strong interaction between Ce<sup>3+</sup> and Tb<sup>3+</sup> (i.e., Ce<sup>3+</sup>-to-Tb<sup>3+</sup> energy transfer), Tb<sup>3+</sup> is more easily excited by Ce<sup>3+</sup> than Tb<sup>3+</sup> itself.

The room-temperature emission spectrum of Tb/Ce-AV-22 excited in the Ce<sup>3+</sup> 4f<sup>1</sup> → 5d<sup>1</sup> transition (Figure 4A) exhibits a series of sharp lines assigned to the <sup>5</sup>D<sub>4</sub> → <sup>7</sup>F<sub>2–6</sub> transitions of Tb<sup>3+</sup>, and luminescence from the higher excited states (e.g., <sup>5</sup>D<sub>3</sub>) is not observed, indicating very efficient nonradiative relaxation to the <sup>5</sup>D<sub>4</sub> level. The spectrum also displays a broad band (370–525 nm) attributed to the allowed Ce<sup>3+</sup> 5d<sup>1</sup> → 4f<sup>1</sup> transition. This assignment is based on the Y/Ce<sup>3+</sup> emission spectrum (recorded using the same excitation conditions), which also displays the 370–525 nm band, inset of Figure 4A. The

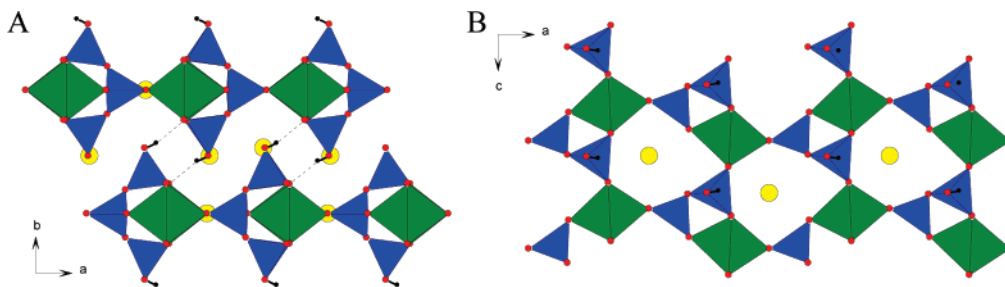


**Figure 2.** (A) Polyhedral representation of Tb-AV-22 viewed along the *c* axis. Dashed lines depict O—H...O bonds. (B) Perforated [TbSi<sub>3</sub>O<sub>8</sub>(OH)<sub>2</sub>]<sup>3-</sup> layer showing K(I) ions (TbO<sub>6</sub>, green; SiO<sub>4</sub>H, SiO<sub>4</sub>, blue; K<sup>+</sup>, yellow ●; O, red ●).

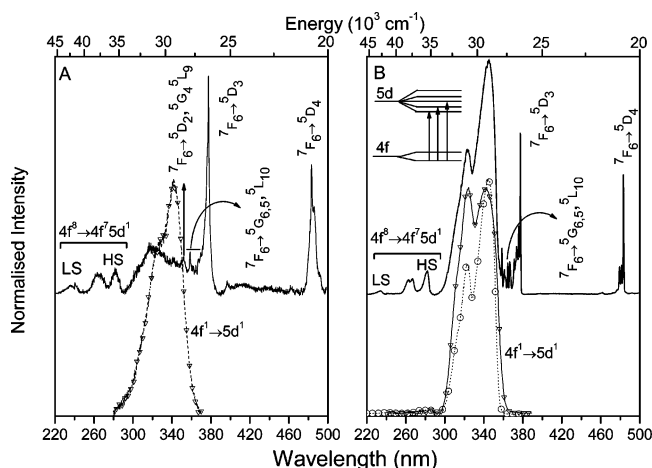


**Figure 3.** (A) Room-temperature excitation spectra of Tb/Ce-AV-22 monitored at 543 nm (solid line) and Y/Ce-AV-22 monitored at 420 nm (▽). (B) 14 K excitation spectra of Tb/Ce-AV-22 monitored at 543 nm (solid line) and 420 nm (○), and Y/Ce monitored at 420 nm (▽).

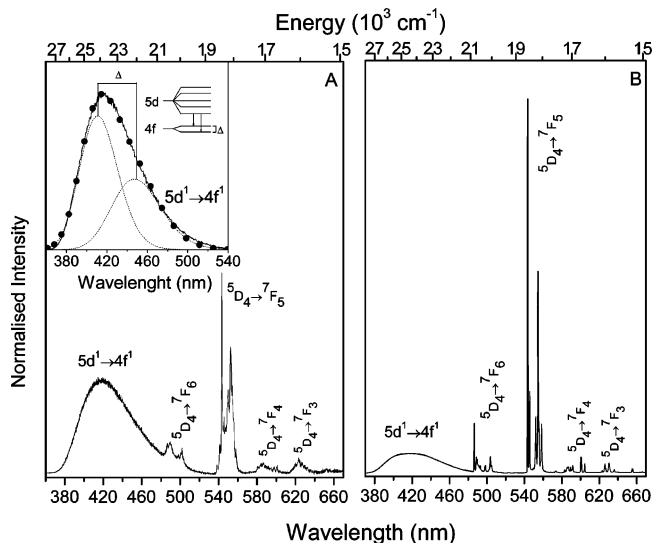


**Figure 4.** (A) Room-temperature and (B) 14 K emission spectra of Tb/Ce-AV-22 excited at 342 nm. The inset shows the Y/Ce-AV-22 room-temperature emission spectrum recorded at 342 nm. Δ ca. 2000 cm<sup>-1</sup> represents the spin-orbit splitting of the Ce<sup>3+</sup> ground state in the <sup>2</sup>F<sub>5/2</sub> and <sup>2</sup>F<sub>7/2</sub> components.

deconvolution of this broad band shows the spin-orbit splitting of the Ce<sup>3+</sup> ground state in the <sup>2</sup>F<sub>5/2</sub> and <sup>2</sup>F<sub>7/2</sub> levels (separated by ca. 2000 cm<sup>-1</sup>). Lowering the temperature to 14 K, the intensity of the 5d<sup>1</sup> → 4f<sup>1</sup> transition decreases, in accord with the increase in the Ce<sup>3+</sup>-to-Tb<sup>3+</sup> energy transfer, as the excitation spectra in Figure 3 suggest. The analysis of the intensity of this Ce<sup>3+</sup> band relative to the Tb<sup>3+</sup> lines makes this point very clear. Upon excitation of the Ce<sup>3+</sup> absorption band,

the spectra in Figure 4 exhibit Ce<sup>3+</sup> and Tb<sup>3+</sup> emissions with relative intensities  $I_{\text{Ce}}:I_{\text{Tb}} = 2.89$  and 1.39, at room temperature and 14 K, respectively. This implies that the Ce<sup>3+</sup>-to-Tb<sup>3+</sup> energy transfer is not complete at the present Ce<sup>3+</sup>/Tb<sup>3+</sup> concentrations and is more efficient at 14 K (we will return to this point later).

The Ce<sup>3+</sup>-to-Tb<sup>3+</sup> energy transfer may take place via radiative transfer, exchange interaction, and electric multipole interaction. The absence in the Ce<sup>3+</sup> emission of f-f Tb<sup>3+</sup> absorption lines (Figure 4) shows that radiative energy transfer between the donor and the acceptor may be neglected. While Ce<sup>3+</sup> and Tb<sup>3+</sup> ions are reducing ions, the exchange interaction would require very high energy, and thus the energy transfer in Tb/Ce-AV-22 should take place, essentially, via electric multipole (dipole-dipole) interaction.<sup>6,9</sup> According to the Dexter theory of energy transfer,<sup>6,9,14</sup> the critical radius for energy transfer by dipole-dipole interaction is defined as the distance for which the probability of transfer equals the probability of radiative emission of the sensitizer and can be obtained by:

$$R_c^6 = 3.024 \times 10^{12} f_d E^{-4} \int f_s(E) F_A(E) dE \quad (1)$$

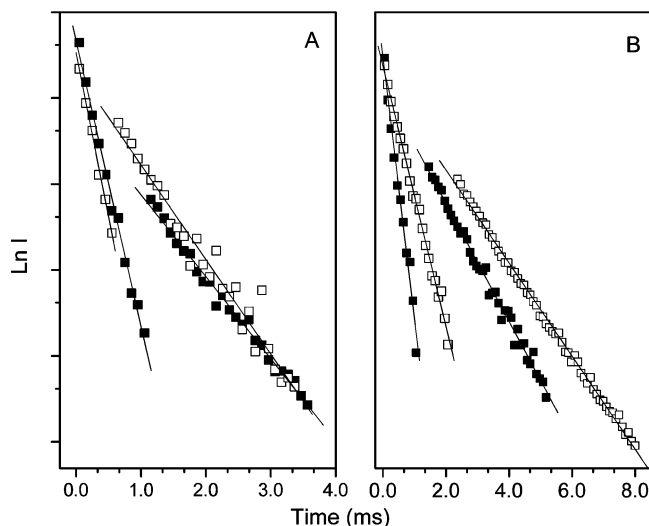
where  $f_d$  of ca.  $10^{-6}$  is the oscillator strength of the Tb<sup>3+</sup> transitions involved in the energy transfer,<sup>9</sup>  $E$  is the energy at maximum spectral overlap,  $f_s$  is the normalized emission line shape function of Ce<sup>3+</sup> (calculated from the inset of Figure 4), and  $F_A$  is the normalized absorption line shape function of Tb<sup>3+</sup> (calculated from the excitation spectrum of Y/Tb-AV-22, Figure 7 of ref 1). The critical distance obtained is ca. 2.71 Å, reflecting the low overlap integral between the emission spectrum of Ce<sup>3+</sup> and the excitation spectrum of Tb<sup>3+</sup>.

The <sup>5</sup>D<sub>4</sub> Tb<sup>3+</sup> lifetimes were monitored as a function of the excitation wavelength and temperature. Figure 5 shows the room-temperature and 14 K <sup>5</sup>D<sub>4</sub> decay curves of Tb/Ce-AV-22 excited on the Tb<sup>3+</sup> levels (377 nm) and on the broad band (342 nm). All <sup>5</sup>D<sub>4</sub> decay curves are biexponential, in perfect agreement with the presence of two distinct local Tb<sup>3+</sup> environments. The corresponding lifetimes are gathered in Table 1. We have previously shown that, whereas Tb-AV-22 sample displays only one local Tb<sup>3+</sup> site, mixed Tb/Eu-AV-22 samples exhibit two distinct Eu<sup>3+</sup> and Tb<sup>3+</sup> local environments.<sup>1</sup> For comparison, the corresponding <sup>5</sup>D<sub>0</sub> and <sup>5</sup>D<sub>4</sub> lifetimes are also listed in Table 1 (the concentration of Eu<sup>3+</sup> in Tb/Eu-AV-22 is similar to that of Ce<sup>3+</sup> in Tb/Ce-AV-22). The incorporation of a small amount of Ce<sup>3+</sup> or Eu<sup>3+</sup> into the Tb-AV-22 structure reduces drastically the <sup>5</sup>D<sub>4</sub> lifetime measured under direct Tb<sup>3+</sup> excitation (377 nm), increasing its dependence with nonradiative effects. This suggests the replacement of Tb<sup>3+</sup> by Ce<sup>3+</sup> (or Eu<sup>3+</sup>) ions into the layers leads to the formation of localized defects, which act as preferential nonradiative recombination regions. However, the existence of two distinct Tb<sup>3+</sup> and Eu<sup>3+</sup> local environments<sup>1</sup> implies that the Ce<sup>3+</sup> (Eu<sup>3+</sup>) ions will also replace K<sup>+</sup> cations



**TABLE 1:**  $^5D_4$  Lifetimes (ms) of Tb/Ce-, Tb/Eu-, and Tb-AV-22 Monitored at 543 nm, Measured for Different Excitation Wavelengths (342 and 377 nm) at 14 and 300 K

	Tb/Ce-AV-22				Tb/Eu-AV-22	Tb-AV-22
	300 K		14 K		300 K	300 K
	342 nm	377 nm	342 nm	377 nm	377 nm	377 nm
$\tau_I$	$1.28 \pm 0.02$	$0.92 \pm 0.02$	$1.63 \pm 0.02$	$1.31 \pm 0.01$	$1.19 \pm 0.02^a$	$4.45 \pm 0.02^a$
$\tau_{II}$	$0.34 \pm 0.01$	$0.22 \pm 0.01$	$0.48 \pm 0.01$	$0.21 \pm 0.01$	$0.68 \pm 0.01^a$	

<sup>a</sup> Values from ref 1; Eu/Tb molar ratio 5%.**Figure 5.** (A) Room-temperature and (B) 14 K  $^5D_4$  decay curves of as-prepared Tb/Ce-AV-22, monitored at 543 nm under (■) 377 nm and (□) 342 nm excitation. The solid lines are the data best linear fit ( $R > 0.99$ ).

residing within the pores of the layers, K(1), and/or interlayer space, K(2). It is not easy to distinguish between these two types of  $Ce^{3+}$  insertion because they induce similar changes in the nearest  $Tb^{3+}$  coordination sphere, due to the similar  $Tb^{3+}$ –K(1) and  $Tb^{3+}$ –K(2) distances (3.68 and 3.83 Å, respectively). According to the critical distance estimated, the efficiency of the  $Ce^{3+}$ -to- $Tb^{3+}$  energy transfer through dipole–dipole interaction ranges from 11% to 15% (for  $Ce^{3+}$  replacing K(1) and K(2) sites) and ca. 1% (for  $Ce^{3+}$  replacing  $Tb^{3+}$  ions located in the layers, average distance of 5.91 Å<sup>1</sup>).

Considering the  $^5D_4$  lifetimes measured for pure Tb-AV-22 and for the mixed Tb/Eu- and Tb/Ce-AV-22 samples (Table 1) and given the small amount of  $Ce^{3+}$  and  $Eu^{3+}$  present in these latter samples, at present we consider that the longer lifetime is attributed to  $Tb^{3+}$  ions in regular crystallographic positions in the layers (site I with lifetime  $\tau_I$ ), whereas the shorter one is ascribed to  $Tb^{3+}$  ions whose coordination sphere was affected by the replacement of  $K^+$  residing in the pores of the layers and/or in the interlayer space by  $Ce^{3+}$  (or  $Eu^{3+}$ ) ions (site II with lifetime  $\tau_{II}$ ). We consider this assignment more correct than the one we have previously proposed.<sup>1</sup> We now discuss the arguments that support this assignment.

The  $^5D_4$  lifetimes decrease as the temperature increases from 14 to 300 K, and this effect depends on the  $Tb^{3+}$  local environment and excitation wavelength (Table 1). On direct intra-4f<sup>8</sup> excitation (377 nm)  $\tau_{II}$  remains essentially constant and  $\tau_I$  decreases ca. 30%, while upon excitation on the  $Ce^{3+}$  levels (342 nm)  $\tau_I$  and  $\tau_{II}$  decrease 20–30%. The larger increase in  $\tau_I$  for direct intra-4f excitation (377 nm) might be explained by the nonradiative components of the two  $Tb^{3+}$  coordination spheres. The contribution of the phonons of the  $[LnSi_3O_8(OH)_2]^{3-}$  layers for the  $Tb^{3+}$  nonradiative deactivation should be larger for site I than for site II. Furthermore, the larger thermal

**TABLE 2:** Room-Temperature Radiance ( $\mu W/cm^2$ ) and (x,y) CIE Color Coordinates for the Standard Green Phosphor  $Gd_2O_2S:Tb$ , Tb-AV-22, and Tb/Ce-AV-22 Measured for Different Excitation Wavelengths (377 and 342 nm)

	Tb/Ce-AV-22		Tb-AV-22	$Gd_2O_2S:Tb$
	377 nm	342 nm	377 nm	270 nm
(x,y)	(0.308, 0.565)	(0.239, 0.236)	(0.336, 0.606)	(0.369, 0.579)
radiance	0.177	0.329	1.804	2.462

activated nonradiative channels for  $\tau_{II}$  excited into the  $Ce^{3+}$  levels should not be associated with the  $^5D_4$  level (attending to the distinct decrease rates as the excitation wavelength changes) and, therefore, should be ascribed to the  $Ce^{3+}$ -to- $Tb^{3+}$  energy transfer mechanisms. The preferential  $Tb^{3+}$  levels ( $^5L_9$ ,  $^5G_4$ ,  $^5D_2$ ) involved in the  $Ce^{3+}$ -to- $Tb^{3+}$  energy transfer are approximately 400–700  $cm^{-1}$  below the lower energy side of the  $4f^1 \rightarrow 5d^1$  transition, whereas the  $^5D_1$  level is located ca. 200  $cm^{-1}$  below the higher energy side of the same  $Ce^{3+}$  transition. As the temperature increases from 14 to 300 K and for an excitation on the  $Ce^{3+}$  levels (342 nm), the  $Tb^{3+}$ -to- $Ce^{3+}$  back-transfer rate may increase, due to phonon-assisted thermally activated mechanisms, in complete agreement with the reported increase in the intensity of the  $5d^1 \rightarrow 4f^1$  transition (Figure 4A). The  $Ce^{3+}$ -to- $Tb^{3+}$  energy transfer may justify the higher  $^5D_4$  lifetimes of both  $Tb^{3+}$  sites for excitation on the  $Ce^{3+}$  levels (342 nm), relative to direct intra-4f<sup>8</sup> excitation (377 nm) (Table 1). Further studies are in progress to fully understand this lifetime dependence.

**3.3. Color Coordinates and Radiance.** The radiance of the  $Gd_2O_2S:Tb$  standard green phosphor, Tb-AV-22, and mixed Tb/Ce-AV-22 samples were measured and compared for different excitation wavelengths (Table 2). At 270 nm excitation, the quantum yield of  $Gd_2O_2S:Tb$  is ca. 95%. The radiances of Tb-AV-22, excited at 377 nm, and  $Gd_2O_2S:Tb$  are of the same order, the former being ca. 25% smaller.

Under direct  $Tb^{3+}$  excitation (377 nm), the Tb/Ce-AV-22 radiance is smaller than the radiance of Tb-AV-22. Because the Tb and Ce contents of both materials are similar, the lower radiance is due to more effective nonradiative channels, as already suggested. Upon 342 nm excitation, the Tb/Ce-AV-22 radiance is about 2 times larger than the radiance measured under direct  $Tb^{3+}$  excitation. This supports the existence of an effective room-temperature  $Ce^{3+}$ -to- $Tb^{3+}$  energy transfer.

The (x,y) emission color coordinates were measured according to the Commission Internationale d'Eclairage (CIE) for the same excitation wavelengths used in the radiance measurements (Table 2). For convenience, the color coordinates of AV-22 materials and the green standard are plotted in the CIE (1931) diagram (Figure 6). Clearly, the Tb-AV-22 and  $Gd_2O_2S:Tb$  color coordinates are similar. The Ce/Tb-AV-22 color coordinates are shifted to the blue, reflecting the  $Ce^{3+}$  blue-band contribution to the overall emission. Although the Ce/Tb-AV-22 radiance is smaller than the pure Tb-AV-22 radiance, the incorporation of  $Ce^{3+}$  allows the tuning of the emission color coordinate from the green to the blue spectral region.

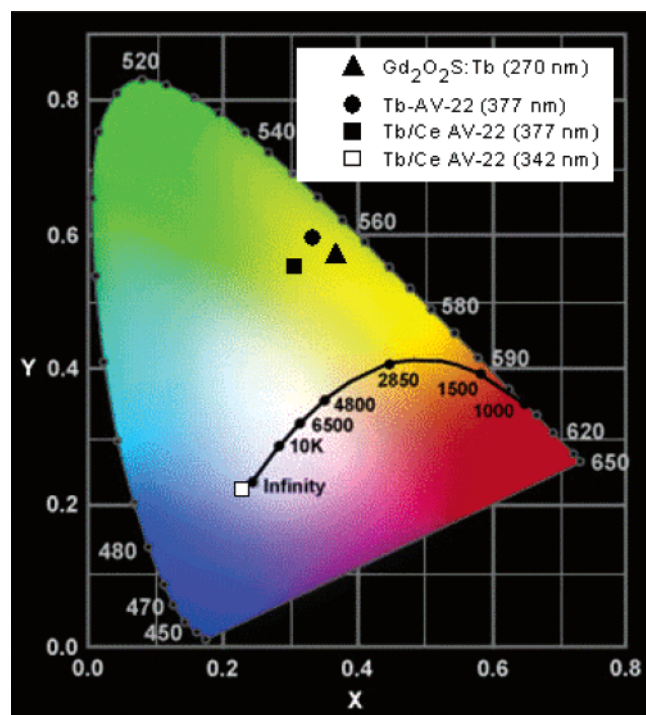


**Figure 6.** CIE chromaticity diagram showing the room-temperature ( $x,y$ ) color coordinates, measured at the excitation wavelengths depicted (see also Table 2).

#### 4. Conclusions

The synthesis and structural characterization of new layered rare-earth silicates  $K_3[M_{1-a}Ce_aSi_3O_8(OH)_2]$ ,  $M = Y^{3+}$ ,  $Tb^{3+}$ ,  $a \ll 1$ , have been reported. In mixed Tb/Ce-AV-22, energy

transfer occurs from the large  $Ce^{3+} 4f^1 \rightarrow 5d^1$  broad band to the sharp  $Tb^{3+} 4f^8$  lines with an efficiency of ca. 15%, estimated assuming the dipole–dipole interaction is the dominant transfer mechanism. Although low, this value enables the fine-tuning of the color emission in the blue-green region of the chromaticity diagram.

**Acknowledgment.** We thank the Portuguese Science Foundation FCT, FEDER and POCTI (POCTI/CTM/46780/02) European programs, and European Network of Excellence FAME. M.H.K. thanks FCT for a Ph.D. grant (SFRH/BD/12323/2003).

#### References and Notes

- (1) Ananias, D.; Kostova, M.; Paz, F. A.; Ferreira, A.; Carlos, L. D.; Klinowski, J.; Rocha, J. *J. Am. Chem. Soc.* **2004**, *126*, 10410.
- (2) Ananias, D.; Ferreira, A.; Rocha, J.; Ferreira, P.; Rainho, J. P.; Morais, C.; Carlos, L. D. *J. Am. Chem. Soc.* **2001**, *123*, 5735.
- (3) Rocha, J.; Ferreira, P.; Carlos, L. D.; Ferreira, A. *Angew. Chem., Int. Ed.* **2000**, *39*, 3276.
- (4) Rocha, J.; Carlos, L. D.; Ferreira, A.; Rainho, J.; Ananias, D.; Lin, Z. *Mater. Sci. Forum* **2004**, *527*, 455.
- (5) Rocha, J.; Carlos, L. D. *Curr. Opin. Solid State Mater. Sci.* **2003**, *7*, 199.
- (6) Hasenkamp, M. F.; Blasse, G. *Chem. Mater.* **1990**, *2*, 105.
- (7) Serra, O. A.; Nassar, D. J.; Zapparolli, G.; Rosa, I. L. V. *J. Alloys Compd.* **1995**, *225*, 63.
- (8) Justel, T.; Wiechert, D. U.; Lau, C.; Sendor, D.; Kynast, U. *Adv. Funct. Mater.* **2001**, *11*, 105.
- (9) You, H.; Wu, X.; Hongtao, H.; Hong, G. *J. Lumin.* **2003**, *104*, 223.
- (10) Lin, J.; Su, Q. *J. Mater. Chem.* **1995**, *5*, 1151.
- (11) Ehrlich, D. J.; Moulton, P. F.; Osgood, R. M. *Opt. Lett.* **1980**, *5*, 339.
- (12) Laroche, M.; Doualan, J. L.; Girard, S.; Margerie, J.; Moncorgé, R. *J. Opt. Soc. Am. B* **2000**, *17*, 1291.
- (13) van Pierterson, L.; Reid, M. F.; Burdick, G. W.; Meijerink, A. *Phys. Rev. B* **2002**, *65*, 045114.
- (14) Dexter, D. L. *J. Chem. Phys.* **1953**, *21*, 836.